Finite Elements in Analysis and Design 215 (2023) 103886

Contents lists available at ScienceDirect

Finite Elements in Analysis & Design

journal homepage: www.elsevier.com/locate/finel

Finite element numerical investigation of multimode ultrasonic interference and beatlengths in high frequency fiber-optic devices: 3D design, modeling, and analysis

Ricardo E. da Silva *, David J. Webb **

Aston Institute of Photonic Technologies, Aston University, Birmingham, B4 7ET, UK

ARTICLE INFO

Keywords:
Spatial-spectral ultrasound analysis
Complex multimode decomposition
Beatlength numerical characterization
3D design optimization
High frequency acousto-optic modulators
Fiber-optic ultrasonic sensors

ABSTRACT

A novel numerical study based on the finite element method is developed to demonstrate the beatlengths induced by high frequency acoustic modes inside an optical fiber for the first time. A practical methodology to model, compute and analyze the multimode interaction in the fiber is exemplified with a detailed numerical experiment. The frequency response of 1 mm long standard fiber is evaluated from 30 to 60 MHz, corresponding to the highest attenuation band of experimental fiber optoacoustic devices. The 3D simulated complex ultrasonic fields are decomposed and characterized with the averaged peak-to-peak method and 2D Fourier transform. The resulting dispersion spectra are compared and theoretically validated by the recognized Pochhammer-Chree solutions. The acoustic parameters required to modulate optical fibers are derived from the simulations and discussed. A route to overcome the frequency-induced limitations of the current devices is provided, pointing out new research possibilities for the development of highly efficient and compact all-fiber acousto-optic modulators and fiber-optic ultrasonic sensors.

1. Introduction

The interaction of sound and light in optical fibers enables important multiphysics applications, such as, all-fiber acousto-optic devices (modulators, dynamic couplers, frequency shifters, notch filters, Q-switched and mode-locked fiber lasers [1–10]) and fiber-optic acoustic sensors (hydrophones, optoacoustic devices for biomedical applications, sensors for high-voltage electric machines, aircrafts, civil infrastructure and vital human signals monitoring [11–18]). In particular, ultrasonic devices composed of fiber Bragg gratings (FBGs) are promising to measure simultaneously acoustic vibrations and temperature [17,19]. The acoustic waves modulate the effective indices of the optical modes and the grating period inducing changes in the Bragg wavelength [20,21]. In this way, electrically-tunable standing longitudinal acoustic waves have been successfully employed to mode-lock the output power of pulsed fiber lasers [9,10,22,23]. The axially symmetric acoustic displacements compress and extend the grating period, inducing reflection bands on both sides of the Bragg wavelength. The grating reflectivity is amplitude modulated by the confined acoustic field in the fiber with a repetition rate at twice the acoustic frequency [24–26]. The modulation of optical fibers employing longitudinal acoustic waves is relatively recent (1997) in comparison with previous studies of cylindrical waveguides [26]. The mathematical model governing the operation of the current acoustic cylinders was first developed independently by Pochhammer in 1876 and Chree in 1889 [27,28]. These studies show that the dispersion phenomenon causes distortion of acoustic waves with wavelengths shorter or in the order of the cylinder diameter [29].

This beating phenomenon is attributed to the different velocities of the modes being excited along the guide at the same frequency [30]. In the last years, significant analytical and semi-analytical models have been developed to predict, understand and characterize the multimode wave propagation in semi-infinite and finite cylindrical geometries based on the Pochhammer-Chree frequency equations [31–33]. The studies indicate that modes propagating with distinct velocities along a dispersive medium travel and arrive at different times, broadening and distorting the shape of acoustic signals [15,32]. The analytical methods evaluate individually the modes and the dominance of one mode over the others at specific frequencies. However, these methods consider only the averaged input and output acoustic fields at the waveguide ends, neglecting the beatlengths induced by the modal interference over the

* Corresponding author.
** Corresponding author.
E-mail addresses: r.da-silva@aston.ac.uk (R.E. da Silva), d.j.webb@aston.ac.uk (D.J. Webb).

https://doi.org/10.1016/j.finel.2022.103886
Received 1 May 2022; Received in revised form 15 November 2022; Accepted 16 November 2022
Available online 25 November 2022

guide cross section. In addition, the radial displacements composing the acoustic modes are usually disregarded during the modeling because the insensitivity of the employed transducers to measure radial variations [32].

Dispersion curves of multiple acoustic modes propagating in an optical fiber have been computed with the Pochhammer-Chree frequency equation to show the change of the phase velocity with the frequency. Nevertheless, the study emphasizes only the fundamental acoustic mode propagating at frequencies lower than 10 MHz [34]. The lack of numerical studies at higher frequencies has limited the current development of fiber-based ultrasonic modulators since the induced multimode interference changes drastically the acousto-optic interaction in the fiber core. Moreover, modeling of the acoustic wave propagation in optical fibers is still highly complex employing the traditional Pochhammer-Chree solutions. The inclusion of boundary conditions to simulate the acoustic transmitter and receiver at the guide ends employing the current analytical methods, usually requires the use of an elaborate mathematical formulism [32,35]. The 2D or 3D evaluation over the guide cross section is too elaborate or even impossible in some cases. In addition, the analytical solutions developed for ideal, homogeneous and solid cylinders cannot be applied for optical fibers with complex geometries, such as, microstructured fibers and photonic crystal fibers [36–38].

Alternatively, semi-analytical finite element method (FEM) can analyze wave propagation in complex waveguides, where the idea was widespread by Kausel since the 1980's with the name of thin layer method [39]. FEM in combination with the computer-aided design (CAD) tools is effective for the development of acoustic and photonic devices [15,36–38,40–44]. In particular, the FEM-based numerical methods are useful for the design, simulation and fabrication of acoustic components, such as, piezoelectric transducers [43,45] and acoustic horns [41,46], allowing multiphysics evaluation of whole acousto-optic devices [47,48]. The interaction of acoustic modes in optical fibers has recently been identified by a FEM-based numerical investigation in the short frequency range from 50 to 56 MHz [49]. The results indicate that the modal superposition causes high distortion of the acoustic fields, resulting in complex non-sinusoidal waveforms in the fiber core.

In this paper, we numerically investigate the beatlengths induced by the complex modal interference with focus on the commonly available and widely employed single-mode standard optical fiber (SMF). The dispersion of the acoustic modes is fully characterized along 1 mm fiber length in the highly dispersive frequency range from 30 to 60 MHz. A brief introduction about the Pochhammer-Chree theory and the resulting frequency equation used to validate the simulations is provided in Section 2. Important acoustic parameters and beatlengths derived from the study are also discussed. A methodology for the design, modeling, and characterization of the 3D fiber geometry by means of the finite element method is described in Section 3. In Section 4, the acoustic period of the modes is evaluated from the acoustically induced displacements with the 2D fast Fourier transform (FFT). In Section 5, the dispersion relation of the wavelength and frequency is analyzed in the FFT spectrum to identify the individual modes and main beatlengths. The spectrally derived acoustic parameters are then employed to analyze the complex modal distribution inside the fiber in Section 6. The dominance of the acoustic modes and the resonant confinement of energy in the fiber core are also discussed. A route to evaluate the modulated optical properties in the SMF and advance the development of high frequency fiber-optic ultrasonic modulators and sensors based on the FEM investigation is discussed in Sections 6.2 and 7.

2. Theoretical background

The Pochhammer-Chree theory describes the wave propagation of acoustic modes in linearly elastic, homogeneous, isotropic and solid cylinders [27,28]. The three-dimensional equations of motion are solved into cylindrical coordinates to define the axially symmetric vibration modes in an infinitely long circular geometry. In particular, the longitudinal acoustic modes induce axially symmetric radial v and axial w displacements in a standard single mode optical fiber (SMF), as illustrated in the yz fiber cross section in Fig. 1(a)–(c). The displacements change with the fiber radial distance r from the fiber core center ($r = 0$) to the fiber surface ($r = 62.5$ μm). The displacement vector $\mathbf{u}$ is decomposed into radial (v for the y axis or u for the x axis) and axial w components defining a set of stress equations [50]. The application of traction-free boundary conditions at the cylindrical surface results in the Pochhammer-Chree frequency equation, which is expressed in terms of the fiber radius a and angular frequency ω as [31,51,52],

$$k^2\frac{qJ_0(qa)}{J_1(qa)}-\frac{1}{2a}\left(\frac{\omega}{c_T}\right)^2+\left[\frac{1}{2}\left(\frac{\omega}{c_T}\right)^2-k^2\right]^2\frac{J_0(pa)}{pJ_1(pa)}=0 \tag{1}$$

in which, $p^2 = \omega^2 c_D^{-2} - k^2$, $q^2 = \omega^2 c_T^{-2} - k^2$, c_D and c_T are respectively the dilatational and transversal acoustic velocities, $\omega = 2\pi f = kc_P$ is the angular frequency, c_P is the phase velocity, $k = 2\pi\lambda_a^{-1}$ is the wavenumber and, λ_a, is the wavelength. J_0 and J_1 are the zero and first order Bessel functions of the first kind (full derivation of Eq. (1) in Achenbach, Zemanek or Redwood [30,50,51]). The frequency equation provides the dispersion relation of the wavenumber k and frequency f for the acoustic modes of a cylindrical geometry. The spectral response k - f is often numerically computed for each mode by solving the roots of Eq. (1). The modal wavenumber or propagation constant k is a real number for the propagating modes.

Fig. 1(d) shows the dispersion of the fundamental acoustic mode $L(0,1)$, and of the second and third higher order modes $L(0,2)$ and $L(0,3)$ in the SMF for a frequency range up to $f = 60$ MHz. The phase velocities c_P (solid lines) and group velocities c_g (dashed lines) of the axially symmetric modes are computed with the wavenumbers k solved from the roots of Eq. (1), employing the methods and algorithms developed in Refs. [31–33,35]. The dispersion curves are compared to the dilatational c_D, transversal c_T and Rayleigh c_R velocities (dotted grey lines). The velocities are normalized in relation to the extensional velocity c_E and indicated with $c_{rel.}$

The acoustic dispersion is also evaluated in terms of the fiber diameter $2a$ considering the dimensionless wavenumber ka [50]. The phase velocity c_P of an acoustic mode approaches the material extensional velocity c_E as $ka \to 0$. Consequently, the displacements induced by

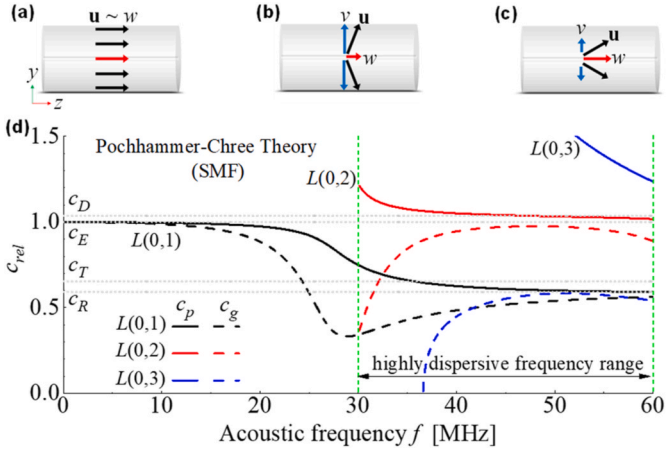

Fig. 1. Illustration of the axial w and radial v displacements acoustically induced in a standard single mode optical fiber (SMF): (a) most of the displacements are axially polarized along the fiber length up to $f = 10$ MHz. (b) Increased transversal polarization of radial components v around $f = 30$ MHz. (c) Predominant alignment of axial components w in the fiber from $f = 40$ - 55 MHz. (d) Pochhammer-Chree dispersion curves indicating the phase velocity c_P (solid lines) and group velocity c_g (dashed lines) of the fundamental mode $L(0,1)$ and higher order acoustic modes $L(0,2)$ and $L(0,3)$ in the SMF.

the fundamental mode $L(0,1)$ are axially distributed over the fiber cross section for the low dispersive frequency range nearly up to 10 MHz, as indicated in Fig. 1(a) and (d). In contrast, c_P approaches the velocity of Rayleigh surface waves c_R as $ka \rightarrow \infty$ [53]. The kinetic energy density E_k of a mode depends on the distribution of its radial and axial displacements over the fiber cross section, propagating along the fiber with the group velocity c_g [34].

Note in the frequency range around $f = 30$ MHz in Fig. 1(d), that modes propagating at lower group velocities induce mostly radial displacements over the fiber cross section, as illustrated in Fig. 1(b). In this range, the fiber cross section also becomes multimode with acoustic periods λ_a comparable to the fiber diameter [54]. Overall, the axial displacements uniformly distributed along the fiber at low frequencies are partially replaced by the radial components, tending to concentrate over the fiber surface with increasing frequency f [34,48,49,55].

The dispersion curves calculated by means of Eq. (1) provide the parameters individually for each acoustic mode. In fact, the acoustic modes interact along the waveguide inducing a complex beatlength pattern [30]. The beatlength or beat wavelength in which the modes exchange energy along the guide is defined as, $B_a = 2\pi(k_i - k_{i+1})^{-1}$, in which, k is the wavenumber and i is the mode index [56–58]. For acoustic modes with wavelengths smaller compared to the guide thickness, the average of the wavenumbers k_i and k_{i+1} approaches the Rayleigh wavenumber as, $k_R = ½(k_i + k_{i+1})$ [57,58]. In this case, the period of the modes converges to the wavelength of Rayleigh waves as, $B_R = 2\pi k_R^{-1}$.

The dispersion of the fundamental mode and the two higher order acoustic modes supported by a SMF is evaluated in the highly dispersive frequency range of $f = 30$ - 60 MHz, corresponding approximately to a high attenuation band in optoacoustic sensors (indicated with the dashed vertical green lines in Fig. 1(d)). The wavelengths λ_a are computed with the modal wavenumbers k provided in Eq. (1). The parameters computed by means of the Pochhammer-Chree frequency equation are named in the next sections as "Theory" to simplify the comparison with the FEM simulations. The theoretical dispersion curves are included in the FEM simulated spectra in terms of the wavelengths λ_a and beatlengths B_a.

3. Three-dimensional FEM design, modeling, and high-performance computing (HPC)

We have modeled a standard single mode optical fiber (SMF-28) with a core diameter of 8.2 μm and a fiber cross section diameter of 125 μm, as illustrated in Fig. 2(a). The fiber is designed by creating a 3D component in the Structural Mechanics Module included in the commercial package COMSOL Multiphysics 5.4, based on the finite element method [59]. An xy work plane (axial coordinate $z = 0$) is defined in the software geometry to model the fiber cross section. The resulting 2D fiber geometry is further extruded along 1 mm length generating a 3D solid cylinder, as illustrated in Fig. 2(b). The fiber is specified as a linear elastic isotropic material with the silica parameters: density $\rho = 2200$ kg/m^3, Young's modulus $Y = 72.5$ GPa and Poisson's ratio $\upsilon = 0.17$ [34,48].

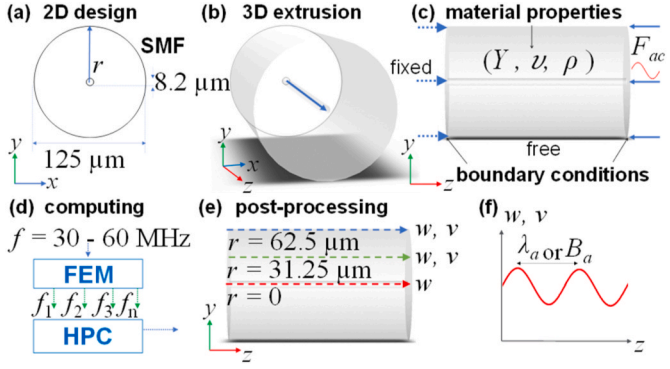

Fig. 2. Modeling of the standard single mode optical fiber (SMF) by employing the finite element method (FEM): (a) The 2D SMF geometry is extruded to generate a (b) 3D solid cylinder. (c) The silica material properties are the Young's modulus Y, Poisson ratio υ and density ρ. The fiber is excited at one end by a sinusoidal force F_{ac} and the other fiber end is fixed. (d) The SMF frequency response is computed by a high-performance computing cluster (HPC) and (e) the acoustically induced axial w and radial v displacements are evaluated over the fiber cross section to calculate the (f) wavelengths of the acoustic modes λ_a and induced beatlengths B_a.

The SMF cross section at the coordinate $z = 1$ mm is axially excited by a sinusoidal force with constant amplitude of $F_{ac} = 3 \times 10^{-3}$ N, in the frequency range from $f = 30$ - 60 MHz, with steps of 100 kHz. The other fiber end is fixed at the coordinate $z = 0$ to provide total reflection of the applied acoustic waves and create a standing acoustic wave pattern (as discussed in Section 1, standing acoustic waves have been employed to modulate the properties of Bragg gratings at twice the acoustic frequency). The remaining fiber surfaces are defined as a free-tension constraint. The summarized boundary conditions are illustrated in Fig. 2(c). The 2D design in Fig. 2(a) is meshed with triangular elements with a maximum element size of 0.3 μm in the fiber core and 10 μm in the cladding. The elements grow symmetrically from the fiber core to the surface with the increasing rate of 1.2. The largest element size is about 6 times smaller than the shortest acoustic wavelength of $\lambda_R = 57$ μm in the frequency range. The element-per-wavelength resolution over the fiber cross section increases with the decreasing radius r approaching to the fiber core. The 2D mesh is further extruded along the fiber length in steps of 10 μm, generating 200 layers of equivalent cross section. It satisfies the mesh element size requirements for accurate FEM modeling, ensuring high resolutions to evaluate the wavelengths and beatlengths in the considered frequency range [59].

The mechanical frequency response of the SMF is computed for each frequency step f by employing the Frequency Domain Study and the Cluster Sweep function available in the software. In this way, each frequency is configured as a "job" and computed by 17 cluster computer nodes. Each node is equipped with 28 processor-cores and memory of 128 GB. The whole frequency response is distributed and solved in parallel by a high-performance computer cluster (HPC), providing a total of 2000 processor-cores and memory of 9 TB, as illustrated in Fig. 2(d). Additional details about modeling of 2D and 3D acousto-optic devices are found in Refs. [6,47,48]. The acoustically induced axial w and radial v displacements are evaluated along the fiber length at the fiber surface ($r = 62.5$ μm) and cladding mid radius ($r = 31.25$ μm), as indicated in Fig. 2(e). At the fiber core center ($r = 0$), only the axial displacements are evaluated since the resulting vector of symmetric radial components is ideally null at this position [34]. Fig. 2(f) illustrates the wavelength of an individual acoustic mode λ_a or beatlength B_a evaluated from the wave envelope computed at the radial distances indicated in Fig. 2(e).

Fig. 3(a) shows an example of the 3D FEM simulation of the SMF excited at the arbitrary frequency of $f = 34.2$ MHz. The acoustically induced displacements are normalized to the maximum positive (dark red color) and negative (dark blue color) amplitudes. A detail of the xy fiber cross section is seen in Fig. 3(b). Fig. 3(c) shows the standing acoustic wave over the yz fiber cross section (indicated as a dashed blue line in Fig. 3(a) and (b)). The displacement modulus $|\mathbf{u}|$ decays to null values at the wave nodes, as indicated by the light green color in Fig. 3(c). The complex wave pattern of $|\mathbf{u}|$ is decomposed into the radial v and axial w components in Fig. 3(d) and (e), revealing distorted periodic waves with periods indicated respectively with λ_1 and λ_2. The acoustic modes causing this complex modal superposition are evaluated and discussed in detail in the next section.

A COMSOL sample file including modeling information employed in the simulations is added as supplementary material. The fiber's geometric and material parameters can be easily changed to simulate

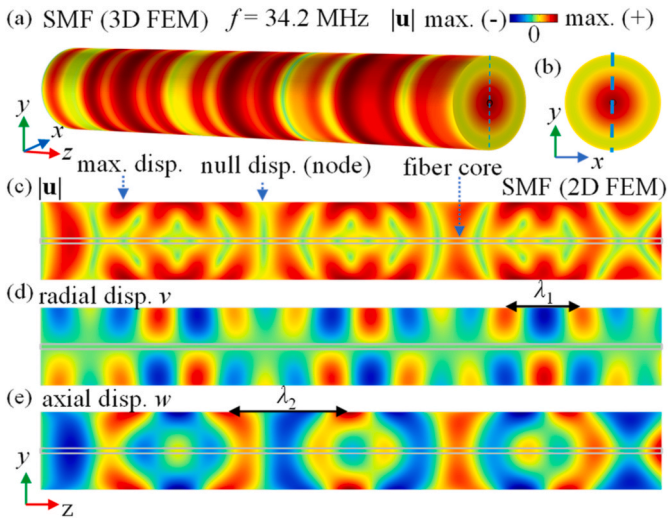

Fig. 3. (a) 3D FEM acoustically induced displacement $|\mathbf{u}|$ along the SMF excited at f = 34.2 MHz with a detail of the (b) xy cross section. (c) $|\mathbf{u}|$ is evaluated over the yz cross section and decomposed into (d) radial v and (e) axial w displacement components.

different fiber devices. This sample can be adapted to run in a desktop computer by accordingly increasing the mesh element size in the fiber cross section mainly in the core region, while considering the mesh requirements detailed in this section.

4. Numerical investigation of the acoustic modal interference in the optical fiber

The period of the FEM simulated acoustic waves is estimated by employing the averaged peak-to-peak method (APP), in which the acoustic wavelength λ_a is calculated by averaging a sequence of half-wavelengths $0.5\lambda_a$ of a standing acoustic wave, corresponding to the distance between the wave nodes [30]. In this study, the APP method additionally measures the distance between sequential wave peaks increasing the measurement accuracy. The overall wavelength λ_a is computed from the averaged distance between the wave nodes and peaks along the fiber.

The interaction of the modes $L(0,1)$ and $L(0,2)$ is predicted at f = 34.2 MHz in Fig. 1(d). Fig. 4 shows examples to evaluate the complex standing wave fields in Fig. 3 with the APP method. The radial v and axial w displacements are assessed at the fiber surface (r = 62.5 μm) and normalized to the maximum amplitude. Note in Fig. 4(a) that a periodic waveform is highly distorted by the modal superposition. Amplitude modulation is clearly seen in the modulus of the radial component v in Fig. 4(b). The same procedure is applied to evaluate the axial displacements w in Fig. 4(c) and (d). The decreased amplitude modulation is followed by a significant period variation $\Delta\lambda_a$ (Fig. 4(c)). The period analysis associated with displacement direction is useful to predict the polarization of the acoustic modes over the fiber cross section. Thus, the lower velocity of $L(0,1)$ towards the transversal and Rayleigh velocities, c_T and c_R, indicates predominant radial polarization over the SMF cross section. Similarly, the larger period and velocity of $L(0,2)$ show that the axial displacements are gradually increasing along the fiber length, implying dominance of this mode with increasing frequency.

Overall, the APP method is more accurate to measure waves with low amplitude modulation. The accuracy increases for waves approaching constant period and amplitude. The simulated wavelengths agree well with the theoretical references, as shown in the details in Fig. 4(b) and (d). The modal wavelengths λ_a and beatlengths B_a are also computed by means of the fast Fourier transform (FFT) [56,57]. The FFT converts the acoustic signal in the space domain (displacement amplitude variation along the fiber length) to the frequency domain (amplitude variation along the spatial frequency $f_z = z^{-1}$) [57]. The resulting FFT spectrum provides the direct and simultaneous measure of the acoustic periods and beatlengths, being useful for the analysis of the polarization, distribution, dominance, and superposition of the modes over the fiber cross section.

For example, the distorted wave fields in Figs. 3 and 4 are also evaluated with the FFT. The modulus of $|v|$ and $|w|$ are sampled along the fiber z-axis with a spatial resolution of Δz = 0.5555 μm, totaling a samples number of N = 1801. The spatial sampling frequency is calculated as, $F_s = \Delta z^{-1} = 1.8\ (\mu m)^{-1}$, resulting in a spatial frequency resolution of $\Delta f_z = F_s N^{-1} = 10^{-3}\ (\mu m)^{-1}$, which is written in function of the spatial resolution as, $\Delta f_z = (N\Delta z)^{-1}$ [60,61]. The number of frequency points in the FFT spectrum is $0.5N$ = 900. The spatially dependent acoustic wavelength $\lambda_a(z)$ is calculated from the inverse values of the spatial frequency components f_z as, $\lambda_a(j) = 2\Sigma(f_z(j))^{-1}$, from $j = 1$ to $j = 0.5N + 1$, where j is the frequency component index. Fig. 5(a) shows the FFT modulus computed from the radial displacements (hollow red

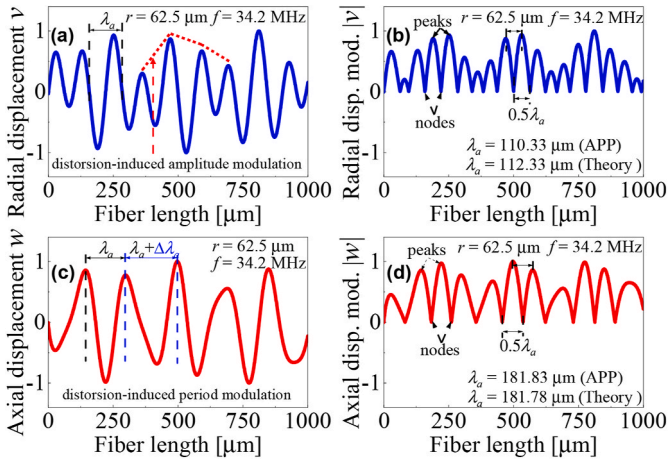

Fig. 4. 1D FEM acoustically induced (a) radial and (c) axial displacements at the SMF surface excited at f = 34.2 MHz. The wavelength of the fundamental mode $\lambda_{L(0,1)}$ and second higher order mode $\lambda_{L(0,2)}$ are respectively estimated from the displacement modulus (b) $|v|$ and (d) $|w|$ with the averaged peak-to-peak method (APP).

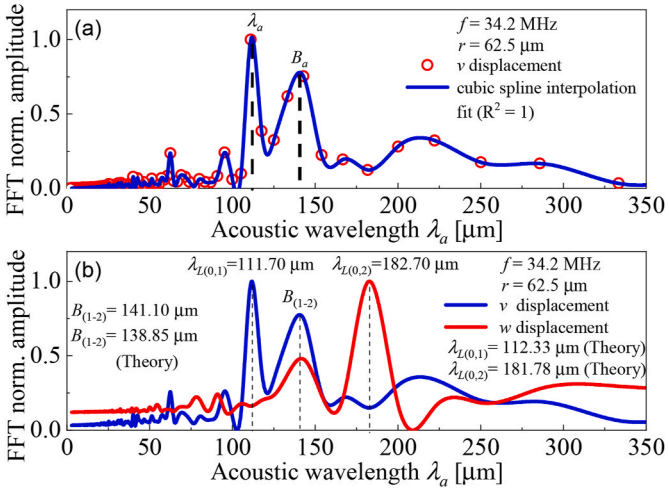

Fig. 5. Example of application of the FFT method to evaluate the complex acoustically induced displacement patterns computed by the FEM. (a) The wavelengths λ_a of the individual acoustic modes and beatlengths B_a are computed from the peaks in the FFT spectrum. (b) FFT of the radial v and axial w displacements in Fig. 4.

circles). The spectrum is normalized to the maximum amplitude. The wavelength λ_a and beatlength B_a are measured directly in the spectrum at the peak's position indicated with vertical dashed lines. The distance between consecutive wavelength λ_a points in the spectrum is written as, $\Delta\lambda_a(j) = \lambda_a(j)j^{-1}$, from $j = 1$ to $j = 0.5N + 1$. The increasing resolution approaching shorter wavelengths λ_a in Fig. 5(a) is caused by natural behavior of the harmonic series in $\lambda_a(j)$. Increasing samples number N is therefore suitable to improve both spatial frequency Δf_z and wavelength $\Delta\lambda_a$ resolution. Alternatively, $\Delta\lambda_a$ is significantly improved by fitting the FFT spectrum with a cubic spline interpolation function, as indicated with the blue curve in Fig. 5(a) [61]. This fitting function provides a constant resolution of $\Delta\lambda_a = 0.1$ μm along the full spectral range, considerably increasing the accuracy to measure the peak's location at wavelengths longer than $\lambda_a = 100$ μm. Fig. 5(b) shows the fitted FFT for both radial and axial displacements. The periods of the fundamental and second higher order mode are respectively indicated at the highest amplitude peaks. The FFT values agree in more than 99% with the theoretical values.

The beatlength of the two modes $B_R(1–2)$ is defined by the smaller peaks in Fig. 5(b). It shows that the modes partially interfere the radial and axial components exchanging energy on the fiber surface [57–59]. In addition, the lower peak at $B_R(1–2)$ indicates that $L(0,2)$ is less distorted by the modal superposition due to its increasing dominance from $f = 34.2$ MHz. The low amplitude oscillations approaching higher values of λ_a indicate the excitation of higher order harmonic components of λ_a and B_a overlapping in the spectrum. Therefore, only the highest resolution peaks with amplitudes higher than 50% in the spectrum are considered to calculate the modal parameters. The method demonstrated in this section is applied to calculate the 2D FFT modal dispersion curves and derive the periods and main beatlengths at the fiber surface, cladding and core.

5. Dispersion analysis of the acoustic modes and beatlengths in the optical fiber

The 2D FFT spectra of the FEM simulated radial and axial displacements at the SMF surface for the frequency range of $f = 30$ - 60 MHz are shown respectively in Fig. 6(a) and (b). The normalized FFT peaks (dark red color) show the period of the acoustic modes λ_a, in comparison with the APP method (white solid line). The FFT-APP spectra in Fig. 6(a) are compared to the Pochhammer-Chree theoretical curves, indicating the period variation of the fundamental acoustic mode $L(0,1)$ and third higher order mode $L(0,3)$ (solid lines), and induced beatlengths B_a (dashed lines). The beats overlapping as Rayleigh waves are indicated as, $B_R(1–2)$ and $B_R(2–3)$, and the second order harmonics as, $B_2(1–2)$ and $B_2(1–3)$. A beating combination of the three modes is indicated as $B_R(1\text{-}2\text{-}3)$. The highest FFT peaks are considered for analysis, as shown with the scattered geometric symbols in Fig. 6(c) and (d). The FEM simulated curves overlap the theoretical values with averaged agreement accuracies higher than 99.9% for all curves in the FFT spectra discussed in this paper.

The overlapping of the FFT-APP curves in Fig. 6(a) indicates high concentration or dominance of $L(0,1)$, which is exchanged or modulated by $B_R(1–2)$ up to about $f = 40$ MHz. The increasing superposition of $L(0,1)$ with the emergent $L(0,3)$ is defined by the beat $B_2(1–3)$ at higher frequencies. These modes propagate with close group velocities considerably lower compared to $L(0,2)$. Similarly, $B_R(2–3)$ is more evident at frequencies higher than $f = 50$ MHz, with decreasing velocity of $L(0,2)$ matching in phase with $L(0,3)$. The dominance of $L(0,2)$ is emphasized by the overlapped FFT-APP curves in Fig. 6(b) and (d). Note in Fig. 6(b) that $L(0,3)$ is not directly detected in the fiber surface, indicating low distribution of this mode and influence of $B_2(1–3)$. The APP dips are caused by a strong resonant coupling of the modes $L(0,1)$ and $L(0,2)$ exchanging with $B_R(1–2)$.

Fig. 7(a) shows the FFT of the radial displacements at the SMF cladding ($r = 31.25$ μm). $B_2(1–3)$ is weakened in the spectrum, implying decreased superposition with $L(0,3)$. As a result, the interference of $L(0,1)$ and $L(0,2)$ is increased by means of $B_R(1–2)$ and $B_2(1–2)$. This second harmonic contributes to broad and low amplitude oscillations in the spectrum. The APP peaks indicate increasing resonant exchange of these modes in this fiber region. In addition, the dominance of $L(0,1)$ in Fig. 6(c) is highly replaced or exchanged with $B_R(1–2)$ in Fig. 7(c). Fig. 7

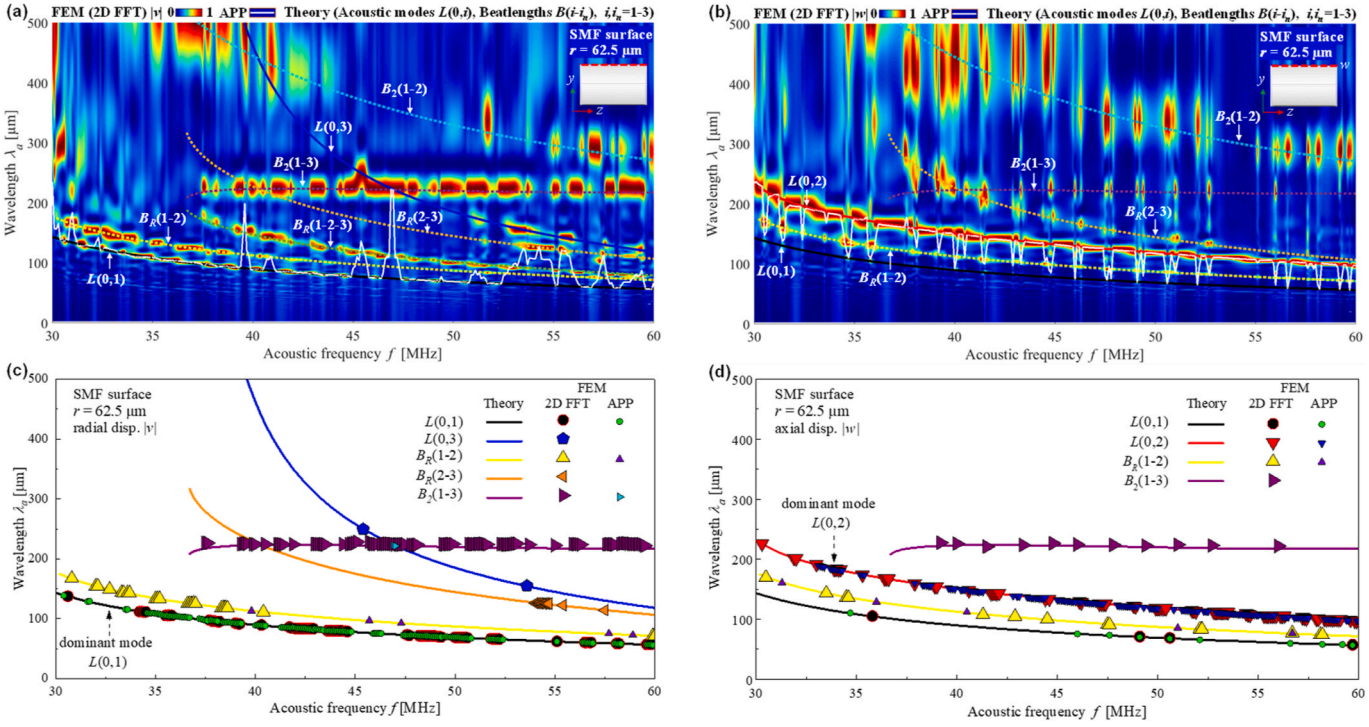

Fig. 6. 2D FFT spectrum of the FEM simulated acoustically induced (a) radial and (b) axial displacements at the SMF surface for $f = 30$ - 60 MHz. (c) (d) The main wavelengths λ_a and beatlengths B_a (scattered geometric symbols) are compared to the theoretical values (solid lines).

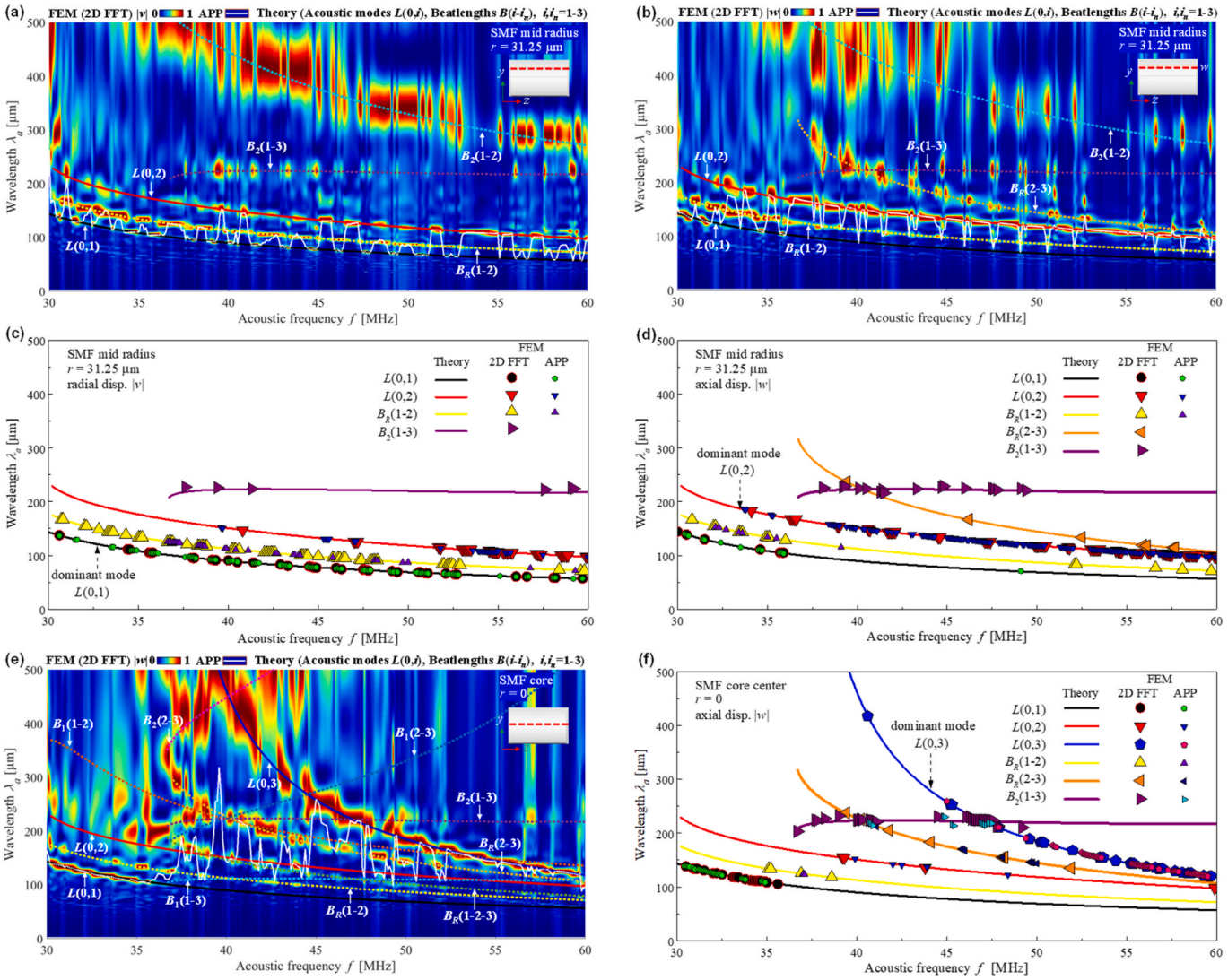

Fig. 7. 2D FFT spectrum of the FEM simulated acoustically induced (a) radial and (b) axial displacements at the SMF cladding for $f = 30$ - 60 MHz. (e) 2D FFT spectrum of the axial displacements at the SMF core for the considered frequency range. (c) (d) (f) The main wavelengths λ_a and beatlengths B_a (scattered geometric symbols) are respectively compared to the theoretical values (solid lines).

(b) shows the spectrum of the axial displacements. For frequencies up to $f = 37$ MHz, the resulting acoustic waves are mostly defined by resonances exchanging the fundamental mode and the beat $B_R(1–2)$.

From $f = 37$ - 50 MHz, the superposition of $L(0,1)$ and $L(0,3)$ reinforces $B_2(1–3)$. Similarly, overlapping of the higher order modes at specific resonances is indicated by $B_R(2–3)$. Note that the intersection of beats, such as, $B_2(1–3)$ and $B_R(2–3)$ around $f = 40$ MHz, reinforces the modal interference. Interactions at higher wavelengths indicate other unrecognized harmonics between the three modes causing low amplitude oscillations. Overall, the resonant dips in Fig. 6(b) decrease with the expansion and dominance of $L(0,2)$ over the fiber cross section with increasing frequency. The high concentration of $L(0,2)$ over the fiber cladding follows the overlapping of the FFT-APP curves in Fig. 7(d).

The spectrum of the axial displacements at the SMF core center is shown in Fig. 7(e). Additional harmonics of the beatlengths are included to provide an intuitive view about the effectiveness of the FEM to simulate the multimode interactions. The relevant beats are summarized in Fig. 7(f). $L(0,1)$ is highly concentrated in the fiber core up to $f = 35$ MHz. At higher frequencies, overlapped beatlengths are seen around $f =$ 40 MHz, mostly governed by $B_R(2–3)$ and $B_2(1–3)$. The increasing dominance of $L(0,3)$ with increasing frequency notably reduces the influence of the beats. Consequently, λ_a approaches the period of $L(0,3)$, as shown by the FFT-APP curves in Fig. 7(f).

In summary, the resonant modal interference and resulting beatlengths change the displacement distribution over the SMF cross section. This frequency-induced modal reallocation is attractive to spatially switch the acoustic energy between the fiber surface, cladding, and core, providing possibilities to convert and filter the modes as discussed in the next section.

6. Analysis of the dominance, spatial redistribution, and energy exchange between the acoustic modes

6.1. Modal dominance and efficiency of energy confinement in the SMF core

We have investigated the dominance of the second higher order mode $L(0,2)$ in the SMF employing the information derived from the FFT spectra. Fig. 8(a) shows the ratio between the axial displacements w and the overall displacements integrated over the SMF cross section along the fiber length (blue curve). The dips in the spectrum correspond to the frequencies where the radial displacements dominate in the fiber. $L(0,2)$

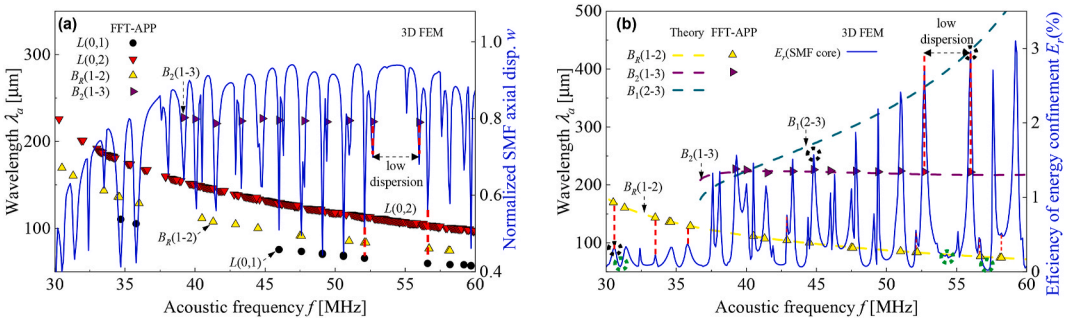

Fig. 8. (a) Normalized axial displacements integrated over the SMF cross section along the fiber length (blue curve) for the frequency range of $f = 30$ - 60 MHz. The dominance of the second higher order acoustic mode $L(0,2)$ is defined at frequencies with high concentration of axial displacements along the fiber. The modal interference causes resonant complex oscillations in the spectrum, being mostly defined by resonances of $L(0,1)$ and the beatlengths between the fundamental and higher order modes $B_R(1–2)$ and $B_2(1–3)$. (b) Efficiency of energy confinement E_r in the SMF core. The resonant frequencies of maximum energy confined in the core are mostly defined by the beatlengths $B_R(1–2)$ and $B_2(1–3)$.

achieves higher group velocities approaching the highest levels of the axial displacement. The wavelengths of $L(0,1)$ and $L(0,2)$ and the beatlengths $B_R(1–2)$ and $B_2(1–3)$ are included for comparison (from FFT-APP curves in Fig. 6(d)). Note that the peaks' frequencies highly agree with the resonant frequencies of $L(0,2)$, weakly interacting with the other modes at the low dispersive frequency range indicated in Fig. 8(a). Otherwise, resonant interference is emphasized between the modes resulting in dips in the spectrum. The smaller dips are caused by the beat $B_2(1–3)$, as indicate at the red dashed lines. In contrast, dips with large depths indicate a strong coupling to $L(0,1)$ and $B_R(1–2)$.

The confinement of acoustic energy inside the SMF core was investigated. The total energy density E_k confined in the fiber core depends on the vector sum of the displacements of each mode interacting in this region. E_k is integrated over the fiber core (E_{co}) and along the entire fiber cross section (E_{cl}). Fig. 8(b) shows the efficiency of energy confinement or acoustic confinement factor $E_r = E_{co}/E_{cl}$ for the considered frequency range (blue curve), denoting the fraction of the overall energy confined in the fiber core. The beats $B_R(1–2)$, $B_2(1–3)$ and $B_1(2–3)$ are included for discussion. The overlapping of $L(0,1)$ and $L(0,2)$ is defined by the beating resonances of $B_R(1–2)$, as indicated by the lower peaks of E_r for frequencies lower than $f = 36.6$ MHz. The low and close group velocities of these radially polarized modes contribute to transfer the energy to the fiber cladding and surface. This interaction decreases with increasing difference of their group velocities and the emergence of $L(0,3)$. The fundamental mode tends to concentrate on the fiber surface while $L(0,2)$ axially polarizes along the fiber with increasing frequency. From $f =$ 36.6 MHz, E_r increases with the emergent $L(0,3)$ highly concentrated in the core, following approximately the growth rate of $B_1(2–3)$. The peak's resonances are mostly defined by $B_2(1–3)$, as shown by the red dashed lines in Fig. 8(b).

Fig. 9 shows the kinetic energy density E_k over the SMF yz cross section at the dip and peak resonances indicated with dashed circles in Fig. 8(b). As discussed, energy is mostly concentrated in the fiber cladding and surface for the resonances in Fig. 9(a) and (b). The beat $B_2(1–3)$ contributes to transfer the energy to the fiber core at $f = 44.8$ MHz in Fig. 9(c). In contrast, the energy is mostly redistributed over the fiber cross section at $f = 54.4$ MHz in Fig. 9(d). The dominant $L(0,2)$ is polarized along the fiber and highly spread over the fiber cross section, reducing energy in the core. Overall, the modal superposition transfers energy between the fiber core and surface at the beating resonances, as shown in Fig. 9(e) and (f). It is analogous to the beatlength resonances investigated in ultrasonic plates, in which the modal interference causes a periodic reflection of energy between the opposite plate surfaces [35, 53,54]. In the SMF, the energy reflects between the fiber surface and core due to the cylindrical geometry. A maximum confinement factor of $E_r = 3.1\%$ is computed at $f = 59.2$ MHz. The characterization of the modal dominance and resonances is important to define the frequency ranges of efficient overlapping of acoustic and optical energy in the fiber

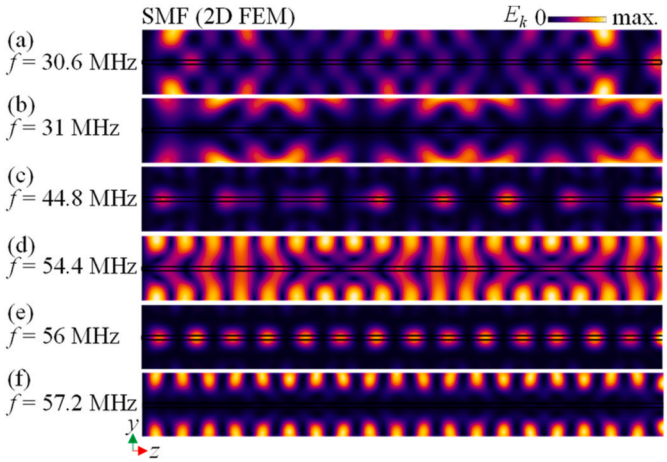

Fig. 9. FEM simulation of the kinetic energy density E_k over the SMF yz cross section at the resonances of (a) $f = 30.6$ MHz, (b) $f = 31$ MHz, (c) $f = 44.8$ MHz, (d) $f = 54.4$ MHz, (e) $f = 56$ MHz and (f) $f = 57.2$ MHz indicated with dashed circles in Fig. 8(b).

core. The predominant longitudinal polarization of the acoustic fields and modal dominance of $L(0,2)$ in the fiber explains the reduced sensitivity of fiber optoacoustic sensors to measure ultrasonic waves transversally polarized on the fiber surface in this frequency range. On the other side, the modal redistribution of the modes over the fiber cross section reveals promising features for mode and spatial-division modulation in acousto-optic devices as discussed in the next section.

6.2. *Evaluation of the complex modal redistribution and frequency-tunable beatlengths inside the SMF*

The beatlength resonances reinforce or attenuate the energy confinement in the fiber core. This *on-off* energy switching is useful for the frequency-tunable modulation of the optical power, and consequently, the electrical control of acousto-optic devices [4]. Similarly, the spectral modal redistribution of the modes in the fiber surface, cladding and core also contributes to increase the detection sensitivity to external substances interacting with the acoustic waves on the fiber surface [7]. In this section, we investigate the variation of the wavelengths and beatlengths caused by the rearrangement of the acoustic modes over the SMF cross section with frequency. Fig. 10 shows an example of wavelength λ_a and beatlength B_a modulation at the arbitrary frequencies of $f = 35$ MHz, $f = 45$ MHz and $f = 55$ MHz. The theoretical curves provide a continuous reference response. The figure analysis reveals the following spatial and spectral modulation possibilities for application in

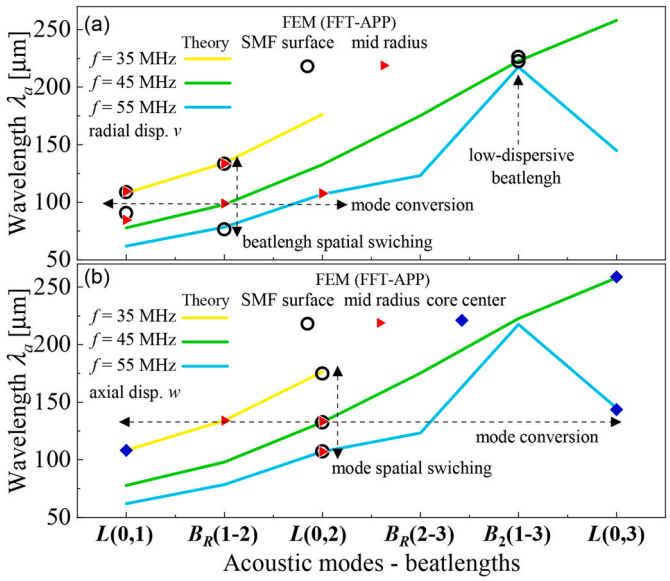

Fig. 10. FEM (FFT-APP) computed wavelength variation of the acoustic modes and beatlengths evaluated by means of the (a) radial v and (b) axial w displacements at the SMF surface (black circle), cladding mid radius (red triangle) and fiber core center (blue square) at the frequencies of $f = 35$ MHz, $f = 45$ MHz and $f = 55$ MHz.

electrically tunable acousto-optic devices:

a) **Frequency-tunable modulation:** The variation of acoustic energy in the fiber core in Fig. 8(b) is followed by significant changes of the acoustic periods and beats in the range $f = 35$ - 55 MHz. It induces a modulation in the spectrum of FBGs, as discussed in Section 1. An almost linear response of λ_a is achieved at specific modal interactions or beats (e.g., $L(0,2)$ and $L(0,3)$ at $f = 45$ MHz in Fig. 10(b)) or even monitoring one mode or beat over the fiber cross section (vertical dashed lines).

b) **Mode conversion:** The horizontal dashed lines in Fig. 10 indicate the exchange of the modes and beatlengths with frequency. For example, $L(0,1)$ distributed in the mid cladding is partially switched to $L(0,2)$ with increasing frequency in Fig. 10(a). Note that λ_a does not considerably change in this case. Fig. 10(b) implies that this modal conversion in the fiber core is suitable to modulate the phase and power of co-propagating optical modes.

c) **Mode or beatlength spatial switching:** The vertical dashed lines in Fig. 10 also indicate redistribution of the modes and beatlengths over the fiber cross section with frequency. For example, $B_R(1–2)$ is highly spread over the fiber cross section at $f = 35$ MHz. This beat is then concentrated in the fiber cladding ($f = 45$ MHz) and surface ($f = 55$ MHz) with increasing frequency. An exception is noted for $B_2(1–3)$ keeping almost constant period and distribution on the fiber surface in the considered frequency range. This feature might be useful to prevent spectral variations caused by broadband acoustic signals in applications modulating the acoustic amplitude.

The 3D FEM simulated displacement patterns in the SMF at the considered frequencies are shown in Fig. 11, with details in the yz fiber cross section. The displacements are decomposed into the radial v and axial w components. The modal wavelengths and beatlengths are evaluated by the FFT-APP methods and indicated at the fiber surface, cladding, and core. It allows the evaluation of the modal spatial distribution in Fig. 10. The color range amplitude is normalized to the maximum of $|\mathbf{u}|$, allowing the qualitative evaluation of the displacement magnitude. At $f = 35$ MHz, $L(0,1)$ and $B_R(1–2)$ dominate over the fiber cladding and surface in Fig. 11(c). $L(0,1)$ mostly moves to the fiber core

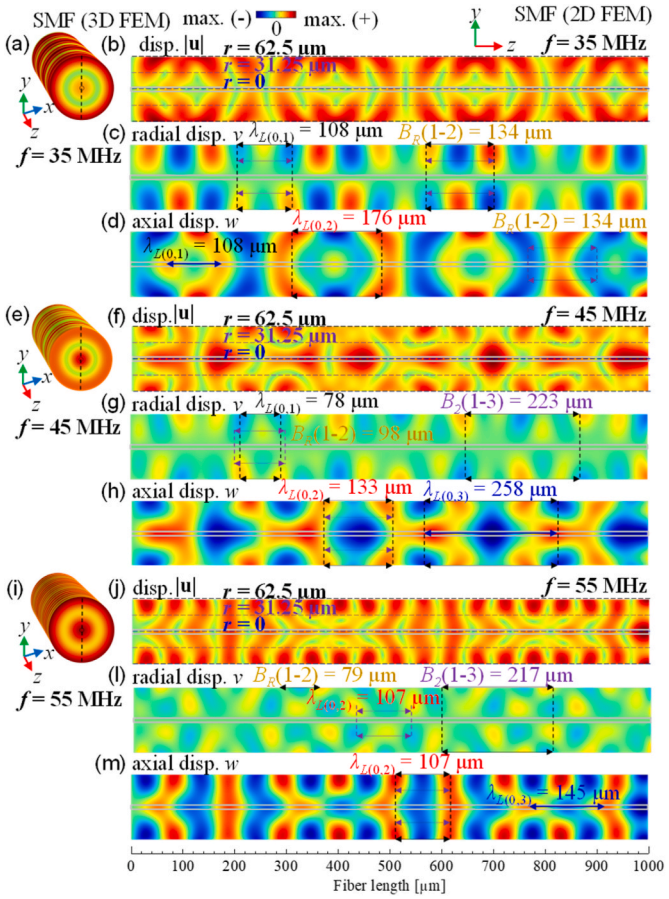

Fig. 11. 3D FEM simulated acoustically induced displacement pattern in the SMF at (a) $f = 35$ MHz, (e) $f = 45$ MHz and (i) $f = 55$ MHz, with details over the SMF yz cross section in Figs. (b) (f) (j). The displacements are decomposed into (c) (g) (l) radial v and (d) (h) (m) axial w components. The wavelengths of the modes and main beatlengths are evaluated by the FFT and APP methods and indicated at the fiber surface ($r = 62.5$ μm), cladding ($r = 31.25$ μm) and core center ($r = 0$).

while $L(0,2)$ emerges on the fiber surface in Fig. 11(d). The modes overlap in the cladding by means of $B_R(1–2)$. These interactions are however weakened by the emergent $L(0,3)$ at $f = 45$ MHz (Fig. 11(g)(h)). The increasing dominance of $L(0,2)$ is seen in Fig. 11(h). Fig. 11(m) shows that the longitudinal modal polarization induces distinct regions of tension (dark red color) and compression (dark blue color) along the fiber. The formation of plane waves over the fiber cross section is expected at frequencies where the mode's velocity approaches the extensional velocity c_E [33]. Consequently, the displacement magnitude of the dominant mode achieves the highest values at these frequencies. Overall, wave distortion is still observed in the fiber core caused by the high concentration of $L(0,3)$. The reduced modal overlap decreases the energy confined in the fiber core, indicating that the beatlengths are therefore required to maximize the energy at any specific region inside the fiber. The beats $B_R(1–2)$ and $B_2(1–3)$ are therefore significant to transfer the energy from the fiber surface and cladding to the fiber core.

7. Results discussion and research outlook for the development of high frequency fiber-optic ultrasonic devices based on the FEM simulations

This study provides a detailed methodology to simulate and analyze complex high frequency ultrasonic fields in optical fibers. Fig. 5 shows an example of a 1D FFT of the distorted acoustic waveforms evaluated at one single frequency in Fig. 4. Note that no useful information can be

directly inferred from Fig. 4; in contrast, the 1D FFT in Fig. 5(b) directly shows the existence of two modes (highest peaks) and one beatlength (overlapped central peak) caused by their modal interference. These modes and beat are uniquely quantified by their periods or wavelengths, which can be expressed in terms of other important parameters, such as, wavenumbers, velocities, or impedances, usually required for ultrasonic applications. Nevertheless, the modes' number and parameters change with frequency. Figs. 6 and 7 show therefore these changes for each frequency in the considered range (the peaks' maximum amplitude in Fig. 5 is indicated as the red color in the 2D FFT). The modal properties are evaluated at the fiber surface, cladding, and core because the distribution of modes and beats also changes in the fiber cross section. Fig. 11 shows an example on how the modes and beats spatially relocate inside the fiber with frequency. The combined spectral and spatial details allow the characterization of modal interactions inside the fiber at a single frequency or range. It is useful to increase the modulation efficiency of inscribed devices in the fiber, such as with π-FBGs employed in optoacoustic sensors with effective sensing lengths of 270–350 μm [14,62]. The spatial modal analysis can show the regions of high concentration of displacements, strains, and overall acoustic energy in the fiber core, indicating the proper position of FBGs to improve the sensor's sensitivity. Similarly, the simulations can assist in the location of the acoustic sources to focus the acoustic waves on the fiber surface.

The demonstrated FEM simulations are promising to assist the development of passive fiber-optic acoustic sensors, such as, optoacoustic devices for biological and medical applications. These sensors have strong potential for minimally invasive high resolution ultrasound imaging, microscale real-time monitoring and diagnosis of diseases in tissues, organs and vessels [13,14,62,63]. In this case, the optical properties are modulated by ultrasonic waves generated within the tissue due to thermoelastic expansion. The acoustically induced strains change the fiber length and the refractive index in the fiber cross section, inducing an optical phase-shift in the propagating optical modes [14,64]. The sensor response is proportionally strong to the axial components because of the high sensitivity to the fiber length variation. Nevertheless, the sensor's response is dominated by transversal resonances around 22 - 30 MHz and 70 - 80 MHz [14,62,63]. Consequently, relevant attenuation of more than 90% of the sensor's sensitivity is experimentally observed in the range of $f = 40$ - 60 MHz. These resonant features cause image distortions and artifacts, usually requiring additional and expensive fiber, electronic or acoustic amplifiers to measure highly attenuated ultrasonic signals. This numerical study is therefore focused on this attenuation range, providing unprecedented details of its multimode cause, as well as useful parameters for further improvements of sensitivity and frequency bandwidth. Other important acoustic parameters, such as, the strain components required to evaluate optical parameters are also directly derived from the FEM [48].

We have simulated the first radial resonance observed in practical optoacoustic sensors to show another example of application of this study. A 1 cm long SMF is modeled by employing the method, fiber parameters and excitation force described in Section 3. The fiber is acoustically excited from $f = 20$ - 40 MHz (1 MHz step), and the corresponding frequency response is computed in terms of the induced radial strains integrated in the fiber core (y direction). Fig. 12 shows the resonance spectrum with a maximum at $f = 29$ MHz. Note that the strain abruptly attenuates with increasing frequency. The FEM simulated resonance peak in Fig. 12 agrees closely with the experimental resonance reported in Ref. [62] (Fig. 2(b)). Differences between the simulated and measured peaks and bandwidths are caused by the influence of distinct boundary conditions and interaction lengths. Overall, the good agreement between the results clearly indicates that the acoustic resonances inside the SMF strongly depend on the fiber geometry, material, and its acoustic modes, regardless of the ultrasonic source, surrounding fiber medium and other components or devices employed in the experimental setup.

The considered resonance is caused by a strong interaction of the

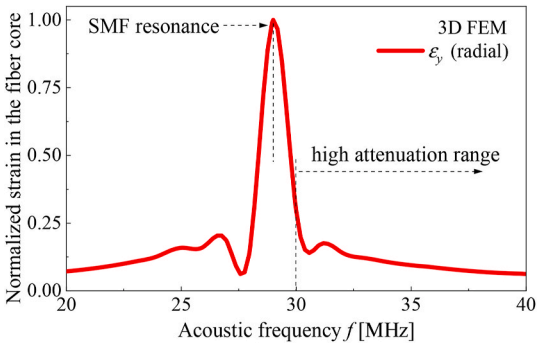

Fig. 12. 3D FEM simulation of the acoustically induced radial strain integrated in the fiber core for the frequency range of $f = 20$ - 40 MHz indicating the first radial ultrasonic resonance of the SMF.

acoustic modes $L(0,1)$ and $L(0,2)$ by means of the beats $B_R(1–2)$ and $B_2(1–2)$. As previously discussed in Fig. 1, these modes have similar, low group velocities at resonance frequencies, in which the displacement fields are resonant and radially polarized within the fiber cross section. For the considered ideal modeled SMF, the strain in the fiber core is significantly reduced with increasing frequency from $f = 30$ MHz. We have shown that the high attenuation band from $f = 40$ - 60 MHz nearly coincides with the range of the dominant second higher order mode $L(0,2)$. The increased axial displacements spread over the fiber cross section are followed by decreased radial or transversal strains in the fiber core, consequently reducing the sensor's sensitivity.

The FEM therefore provides a complete tool to characterize ultrasonic fields inside the SMF in comparison with the current analytical or semi-analytical methods based on the scattering of elastic waves [14,63]. It is expected that the conversion of the spherical acoustic waves into only axially symmetric waves will reinforce the axial displacements in the fiber core. The FEM simulated strain in the core can be used in combination with analytic methods (e.g., the transfer matrix method) to model the properties of Bragg gratings, providing the optical spectral response for the devices [47,48]. Similarly, components surrounding the fiber, such as, fiber coatings, acoustic sources and sensing substances are directly modeled employing the method described in Section 3, just by adding the component geometries, materials and physical domains [6,47,65]. In this sense, phase and group velocities c_P and c_g, can be derived from λ_a to calculate acoustic impedances to match with surrounding components, enabling efficient integration with the acoustic and photonic devices.

Optical fibers with complex geometries also benefit from these modeling features [49]. Further numerical research should involve the simulation of propagating acoustic waves in the SMF and the time representation of the dispersed signals at high frequencies, which is obtained with the inverse Fourier transform of the frequency spectra. This is achieved by employing a time-dependent study in combination with a perfectly matched layer (PML) as an absorbing boundary condition [59].

Overall, changes in the fiber cross section design, diameter or material composition are required to adjust the modal beatlengths, enabling possibilities to improve the sensor's sensitivity towards a flat response over a broadband frequency range. It might be achieved by improved filtering of acoustic modes employing a permanent periodic mechanical deformation along the SMF (e.g., inscription of FBGs and long period gratings (LPGs) by changing periodically the fiber material or diameter with a CO_2 or femtosecond laser [66,67]). In Photonics, the reflection or transmission properties of these gratings strictly depend on the fiber's optical modal properties and spectral response, usually quantified by the modes' effective indices. Similarly, the development of gratings for application as ultrasonic filters relies on previous knowledge of acoustic modal properties. This study therefore provides significant modal parameters which can be estimated directly from the FFT dispersion curves in Figs. 6 and 7 for the considered frequency range.

The evaluated modal wavelengths λ_a can be expressed in terms of wavenumbers k to assist in design and fabrication of emergent FBGs and LPGs specifically for ultrasound. Broadband chirped gratings are promising to equalize the spectrum of resonances and attenuation bands over a wide frequency range, analogous to their photonic counterparts [7]. These gratings might be designed and simulated by considering proper periodic variation of material or diameter along the SMF modeled in Section 3. The resulting grating spectrum and changes in modal interaction might be evaluated by means of the FFT spectra or frequency response of the fiber, e.g., as shown in Fig. 12.

Alternatively, optical fibers with reduced fiber cross section will contribute to reduce the number of modes and minimize the distortion caused by dispersion in the range of $f = 30$–60 MHz (the fiber diameter should be considerably smaller compared to the acoustic wavelength). In this way, low dispersive or dispersionless single-mode acoustic devices might be achieved by reduced fiber cross section, employing cladding etching and tapering techniques employed to fabricate photonic devices [24,26,68]. The methodology and findings described in this paper will certainly contribute to evaluate the material and geometric changes along the SMF, allowing the practical modeling and fast evaluation of all-fiber modulators and sensors.

8. Conclusion

In summary, we have numerically investigated the beatlengths induced by axially symmetric acoustic modes inside a standard optical fiber for the first time. A methodology for the design, modeling and analysis of a 1 mm long device employing the 3D finite element method (FEM) is demonstrated. The spectral response of the acoustic modes and beatlengths is computed with the 2D fast Fourier transform (FFT) for the frequency range of $f = 30$ - 60 MHz. The induced radial and axial displacements are evaluated at the fiber surface, cladding and core, allowing the characterization of the fundamental acoustic mode $L(0,1)$ and the two higher order modes $L(0,2)$ and $L(0,3)$ by means of the dispersion spectra. The FEM simulated dispersion responses are compared to the Pochhammer-Chree analytical solutions with accuracies higher than 99.9%.

The beatlengths, modal dominance and displacement distribution are assessed over the 2D fiber cross sections of the simulated device. The results indicate dominance of $L(0,2)$ with increasing polarization of the axial components along the fiber. It is followed by a surprising decrease of acoustic energy in the fiber core, mostly governed by resonant beatlengths. Increasing interference of the three modes is therefore suitable to increase in-core modulation. For frequencies higher than $f = 60$ MHz, the dominance of $L(0,3)$ and the occurrence of new higher order modes is expected. The revealed beatlength-induced acoustic gratings in combination with the frequency-tuning features described in Section 6 are promising to increase the acousto-optic interaction in the fiber cross section, enabling highly efficient modulation of higher order optical modes.

Overall, the FEM provides a graphical and intuitive tool to investigate the dispersion and modal interference inside optical fibers. Important details for 2D and 3D design, physical modeling, computing and post-processing required to evaluate experimental devices with high accuracy and resolution are provided. We expect that the research findings and guidelines described by this numerical investigation will contribute for the development and characterization of high frequency devices based on the commonly used SMFs. These procedures can be additionally employed to model any cylindrical geometry, as well as optical fibers with complex designs, such as, microstructured and photonic crystal fibers, in which the current analytical or semi-analytic methods are not possible. The simulated acoustic parameters enable further evaluation of the modulated grating properties in devices employing FBGs. The numerical investigation points out a way to overcome the frequency limitation of the current acousto-optic modulators and improve the noise-limited pressure resolution of optoacoustic sensors, contributing to compact and efficient all-fiber devices.

Credit author statement

Ricardo E. da Silva: Investigation, Methodology, Formal analysis, Validation, Writing – original draft, Writing – review & editing. **David J. Webb:** Investigation, Writing – review & editing, Funding acquisition, Resources.

Declaration of competing interest

The authors declare that they have no known competing financial interests or personal relationships that could have appeared to influence the work reported in this paper.

Data availability

Data will be made available on request.

Acknowledgements

This project has received funding from the European Union's Horizon 2020 research and innovation programme under the Marie Sklodowska-Curie grant agreement No 713694. We acknowledge the use of Athena at HPC Midlands+, which was funded by the EPSRC on grant EP /P020232/1 as part of the HPC Midlands+ consortium.

Appendix A. Supplementary data

Supplementary data to this article can be found online at https://doi.org/10.1016/j.finel.2022.103886.

References

[1] J.N. Blake, B.Y. Kim, H.E. Engan, H.J. Shaw, Analysis of intermodal coupling in a two-mode fiber with periodic microbends, Opt. Lett. 12 (1987) 281, https://doi.org/10.1364/OL.12.000281.
[2] T.A.T. Birks, P.S.J. Russell, D.O. Culverhouse, The acousto-optic effect in single-mode fiber tapers and couplers, J. Lightwave Technol. 14 (1996) 2519–2529, https://doi.org/10.1109/50.548150.
[3] S.H. Yun, I.K. Hwang, B.Y. Kim, All-fiber tunable filter and laser based on two-mode fiber, Opt. Lett. 21 (1996) 27–29, https://doi.org/10.1364/OL.21.000027.
[4] R.E. Silva, E. Manuylovich, N. Sahoo, M. Becker, M. Rothhardt, H. Bartelt, D. J. Webb, Highly efficient side-coupled acousto-optic modulation of a suspended core fiber Bragg grating, IEEE Photon. Technol. Lett. 33 (2021) 1379–1382, https://doi.org/10.1109/LPT.2021.3123258.
[5] J. Lu, F. Shi, J. Xu, L. Meng, L. Zhang, P. Cheng, X. Zhou, F. Pang, X. Zeng, Recent progress of dynamic mode manipulation via acousto-optic interactions in few-mode fiber lasers: mechanism, device and applications, Nanophotonics 10 (2021) 983–1010, https://doi.org/10.1515/nanoph-2020-0461.
[6] I.B. Javorsky, R.E. Silva, A.A.P. Pohl, Wavelength tunable filter based on acousto-optic modulation of a double-core fiber, IEEE Photon. Technol. Lett. 31 (2019) 1135–1138, https://doi.org/10.1109/LPT.2019.2919483.
[7] A.A.P. Pohl, R.A. Oliveira, R.E. Silva, C.A.F. Marques, P. de T. Neves, K. Cook, J. Canning, R.N. Nogueira, Advances and new applications using the acousto-optic effect in optical fibers, Photonic Sensors 3 (2013) 1–25, https://doi.org/10.1007/s13320-013-0100-0.
[8] R.E. Silva, M. Becker, M. Rothhardt, H. Bartelt, A.A.P. Pohl, Acousto-optic double side-band amplitude modulation of a fiber Bragg grating in a four-holes suspended-core fiber, J. Lightwave Technol. 36 (2018) 4146–4152, https://doi.org/10.1109/JLT.2018.2856079.
[9] R.E. Silva, T. Tiess, M. Becker, T. Eschrich, M. Rothhardt, M. Jäger, A.A.P. Pohl, H. Bartelt, Acousto-optic modulation of a fiber Bragg grating in suspended core fiber for mode-locked all-fiber lasers, Laser Phys. Lett. 12 (2015), 045101, https://doi.org/10.1088/1612-2011/12/4/045101.
[10] I.L. Villegas, C. Cuadrado-Laborde, J. Abreu-Afonso, A. Díez, J.L. Cruz, M. A. Martínez-Gámez, M.V. Andrés, Mode-locked Yb-doped all-fiber laser based on in-fiber acoustooptic modulation, Laser Phys. Lett. 8 (2011) 227–231, https://doi.org/10.1002/lapl.201010116.
[11] N.E. Fisher, D.J. Webb, C.N. Pannell, D.A. Jackson, L.R. Gavrilov, J.W. Hand, L. Zhang, I. Bennion, Ultrasonic hydrophone based on short in-fiber Bragg gratings, Appl. Opt. 37 (1998) 8120, https://doi.org/10.1364/ao.37.008120.
[12] G.M. Ma, H.Y. Zhou, C. Shi, Y.B. Li, Q. Zhang, C.R. Li, Q. Zheng, Distributed partial discharge detection in a power transformer based on phase-shifted FBG, IEEE Sensor. J. 18 (2018) 2788–2795, https://doi.org/10.1109/JSEN.2018.2803056.

[13] A. Rosenthal, D. Soliman, G. Wissmeyer, R. Shnaiderman, V. Ntziachristos, All-optical optoacoustic microscope based on wideband pulse interferometry, Opt. Lett. 41 (Issue 9) (2016) 1953–1956, https://doi.org/10.1364/OL.41.001953, 1953–1956.
[14] I.A. Veres, P. Burgholzer, T. Berer, A. Rosenthal, G. Wissmeyer, V. Ntziachristos, Characterization of the spatio-temporal response of optical fiber sensors to incident spherical waves, J. Acoust. Soc. Am. 135 (2014) 1853, https://doi.org/10.1121/1.4868391.
[15] A. Cusano, P. Capoluongo, S. Campopiano, A. Cutolo, M. Giordano, F. Felli, A. Paolozzi, M. Caponero, Experimental modal analysis of an aircraft model wing by embedded fiber bragg grating sensors, IEEE Sensor. J. 6 (2006) 67–77, https://doi.org/10.1109/JSEN.2005.854152.
[16] W. Ecke, I. Latka, R. Willsch, A. Reutlinger, R. Graue, Fibre optic sensor network for spacecraft health monitoring, Meas. Sci. Technol. 12 (2001) 974, https://doi.org/10.1088/0957-0233/12/7/339.
[17] P. Moyo, J.M.W. Brownjohn, R. Suresh, S.C. Tjin, Development of fiber Bragg grating sensors for monitoring civil infrastructure, Eng. Struct. 27 (2005) 1828–1834, https://doi.org/10.1016/J.ENGSTRUCT.2005.04.023.
[18] L. Dziuda, F.W. Skibniewski, M. Krej, J. Lewandowski, Monitoring respiration and cardiac activity using fiber Bragg grating-based sensor, IEEE Trans. Biomed. Eng. 59 (2012) 1934–1942, https://doi.org/10.1109/TBME.2012.2194145.
[19] Y.J. Rao, D.J. Webb, D.A. Jackson, L. Zhang, I. Bennion, In-fiber bragg-grating temperature sensor system for medical applications, J. Lightwave Technol. 15 (1997) 779–784, https://doi.org/10.1109/50.580812.
[20] P.A. Fomitchov, S. Krishnaswamy, Response of a fiber Bragg grating ultrasonic sensor, Opt. Eng. 42 (2003) 956, https://doi.org/10.1117/1.1556372.
[21] A. Minardo, A. Cusano, R. Bernini, L. Zeni, M. Giordano, Response of fiber bragg gratings to longitudinal ultrasonic waves, IEEE Trans. Ultrason. Ferroelectrics Freq. Control 52 (2005) 304–312, https://doi.org/10.1109/TUFFC.2005.1406556.
[22] C. Cuadrado-Laborde, A. Díez, J.L. Cruz, M.V. Andrés, Experimental study of an all-fiber laser actively mode-locked by standing-wave acousto-optic modulation, Appl. Phys. B 99 (2009) 95–99, https://doi.org/10.1007/s00340-009-3869-1.
[23] C. Cuadrado-Laborde, A. Diez, M. Delgado-Pinar, J.L. Cruz, M.V. Andrés, Mode locking of an all-fiber laser by acousto-optic superlattice modulation, Opt. Lett. 34 (2009) 1111, https://doi.org/10.1364/OL.34.001111.
[24] W.F. Liu, P.S.J. Russell, L. Dong, 100% efficient narrow-band acoustooptic tunable reflector using fiber Bragg grating, J. Lightwave Technol. 16 (1998) 2006, https://doi.org/10.1109/50.730362. –2009.
[25] P.S.J. Russell, W.-F. Liu, Acousto-optic superlattice modulation in fiber Bragg gratings, J. Opt. Soc. Am. A 17 (2000) 1421, https://doi.org/10.1364/JOSAA.17.001421.
[26] W.F. Liu, P.S. Russell, L. Dong, Acousto-optic superlattice modulator using a fiber Bragg grating, Opt. Lett. 22 (1997) 1515–1517, https://doi.org/10.1364/OL.22.001515.
[27] L. Pochhammer, On the velocity of propagation of small vibrations in an isotropic cylinder of infinite length". Ueber die fortpflanzungsgeschwindigkeiten kleiner schwingungen in einem unbegrenzten isotropen kreiscylinder, J. Fur Die Reine Und.Angew. Math. 1876 (1876) 324–336, https://doi.org/10.1515/crll.1876.81.324.
[28] C. Chree, Longitudinal vibrations of a circular bar, Q. J. Pure Appl. Math. 21 (1886) 287–289.
[29] R.M. Davies, A critical study of the Hopkinson pressure bar, Philos. Trans. R. Soc. London. Ser. A, Math. Phys. Sci. 240 (1948) 375–457, https://doi.org/10.1098/rsta.1948.0001.
[30] J. Zemanek, An experimental and theoretical investigation of elastic wave propagation in a cylinder, J. Acoust. Soc. Am. 51 (1972) 265–283, https://doi.org/10.1121/1.1912838.
[31] M.L. Peterson, Prediction of longitudinal disturbances in a multimode cylindrical waveguide, Exp. Mech. 39 (1999) 36–42, https://doi.org/10.1007/BF02329299.
[32] A.D. Puckett, M.L. Peterson, A semi-analytical model for predicting multiple propagating axially symmetric modes in cylindrical waveguides, Ultrasonics 43 (2005) 197–207, https://doi.org/10.1016/j.ultras.2004.04.008.
[33] A.D. Puckett, M.L. Peterson, Individual longitudinal Pochhammer-Chree modes in observed experimental signals, Acoust Res. Lett. Online 6 (2005) 268–273, https://doi.org/10.1121/1.2033088.
[34] H.E. Engan, B.Y. Kim, J.N. Blake, H.J. Shaw, Propagation and optical interaction of guided acoustic waves in two-mode optical fibers, J. Lightwave Technol. 6 (1988) 428–436, https://doi.org/10.1109/50.4020.
[35] A. Puckett, An Experimental and Theoretical Investigation for Axially Symmetric Wave Propagation in Thick Cylindrical Waveguides, 2004. http://digitalcommons.library.umaine.edu/etd/285. (Accessed 13 June 2021). accessed.
[36] B. Stiller, G. Mélin, H. Maillotte, J.-C. Beugnot, M. Delqué, M.W. Lee, T. Sylvestre, V. Laude, Frequency-selective excitation of guided acoustic modes in a photonic crystal fiber, 19, Opt Express 19 (Issue 8) (2011) 7689–7694, https://doi.org/10.1364/OE.19.007689, 7689–7694.
[37] K. Saitoh, M. Koshiba, Full-vectorial imaginary-distance beam propagation method based on a finite element scheme: application to photonic crystal fibers, IEEE J. Quant. Electron. 38 (2002) 927–933, https://doi.org/10.1109/JQE.2002.1017609.
[38] A. Cucinotta, S. Selleri, L. Vincetti, M. Zoboli, Holey fiber analysis through the finite-element method, IEEE Photon. Technol. Lett. 14 (2002) 1530–1532, https://doi.org/10.1109/LPT.2002.803375.
[39] J.L. Tassoulas, E. Kausel, Elements for the numerical analysis of wave motion in layered strata, Int. J. Numer. Methods Eng. 19 (1983) 1005–1032, https://doi.org/10.1002/nme.1620190706.
[40] A.C. Hladky-Hennion, Finite element analysis of the propagation of acoustic waves in waveguides, J. Sound Vib. 194 (1996) 119–136, https://doi.org/10.1006/JSVI.1996.0349.
[41] S.G. Amin, M.H.M. Ahmed, H.A. Youssef, Computer-aided design of acoustic horns for ultrasonic machining using finite-element analysis, J. Mater. Process. Technol. 55 (1995) 254–260, https://doi.org/10.1016/0924-0136(95)02015-2.
[42] P. Hora, O. Červená, Determination of Lamb wave dispersion curves by means of Fourier transform, Appl. Comput. Mech. 6 (2012) 5–16. https://www.kme.zcu.cz/acm/acm/article/view/149. (Accessed 17 September 2021). accessed.
[43] C. Yang, L. Ye, Z. Su, M. Bannister, Some aspects of numerical simulation for Lamb wave propagation in composite laminates, Compos. Struct. 75 (2006) 267–275, https://doi.org/10.1016/J.COMPSTRUCT.2006.04.034.
[44] F. Zangeneh-Nejad, R. Fleury, Acoustic analogues of high-index optical waveguide devices, Sci. Rep. 81 (2018) 1–12, https://doi.org/10.1038/s41598-018-28679-1, 8 (2018.
[45] R.E. Silva, M.A.R. Franco, H. Bartelt, A.A.P. Pohl, Numerical characterization of piezoelectric resonant transducer modes for acoustic wave excitation in optical fibers, Meas. Sci. Technol. 24 (2013), 094020, https://doi.org/10.1088/0957-0233/24/9/094020.
[46] R.A. Oliveira, P.T. Neves Jr., J.T. Pereira, J. Canning, A.A.P. Pohl, Vibration mode analysis of a silica horn-fiber Bragg grating device, Opt Commun. 283 (2010) 1296–1302, https://doi.org/10.1016/j.optcom.2009.11.035.
[47] R.E. Silva, M.A.R. Franco, P.T. Neves, H. Bartelt, A.A.P. Pohl, P. Neves Jr., H. Bartelt, A.A.P. Pohl, Detailed analysis of the longitudinal acousto-optical resonances in a fiber Bragg modulator, Opt Express 21 (2013) 6997–7007, https://doi.org/10.1364/OE.21.006997.
[48] R.E. Silva, A. Hartung, M. Rothhardt, A.A.P. Pohl, H. Bartelt, Detailed numerical investigation of the interaction of longitudinal acoustic waves with fiber Bragg gratings in suspended-core fibers, Opt Commun. 344 (2015) 43–50, https://doi.org/10.1016/j.optcom.2015.01.037.
[49] R.E. Silva, D.J. Webb, Ultra-efficient in-core acoustic waves in suspended core fiber for high frequency fiber-optic ultrasonic devices, APEX 14 (2021), 087003, https://doi.org/10.35848/1882-0786/AC17D5.
[50] J. Achenbach, Wave Propagation in Elastic Solids, first ed., Elsevier Science, 1984.
[51] M. Redwood, Mechanical Waveguides: the Propagation of Acoustic and Ultrasonic Waves in Fluids and Solids with Boundaries, Pergamon Press, New York, 1960. https://catalog.princeton.edu/catalog/9915017573506421. (Accessed 22 September 2021). accessed.
[52] M. Redwood, Velocity and attenuation of a narrow-band, high-frequency compressional pulse in a solid wave guide, J. Acoust. Soc. Am. 31 (2005) 442, https://doi.org/10.1121/1.1907732.
[53] R.N. Thurston, Elastic waves in rods and clad rods, J. Acoust. Soc. Am. 64 (1978) 1–37, https://doi.org/10.1121/1.381962.
[54] D. Bancroft, The velocity of longitudinal waves in cylindrical bars, Phys. Rev. 59 (1941) 588–593, https://doi.org/10.1103/PhysRev.59.588.
[55] R.E. Silva, T. Tiess, M. Becker, T. Eschrich, M. Rothhardt, M. Jäger, A.A.P. Pohl, H. Bartelt, All-fiber 10 MHz acousto-optic modulator of a fiber Bragg grating at 1060 nm wavelength, Opt Express 23 (2015), 25972, https://doi.org/10.1364/OE.23.025972. –8.
[56] B. Masserey, C. Raemy, P. Fromme, High-frequency guided ultrasonic waves for hidden defect detection in multi-layered aircraft structures, Ultrasonics 54 (2014) 1720–1728, https://doi.org/10.1016/j.ultras.2014.04.023.
[57] B.W. Ti, W.D. O'Brien, J.G. Harris, Measurements of coupled Rayleigh wave propagation in an elastic plate, J. Acoust. Soc. Am. 102 (1997) 1528–1531, https://doi.org/10.1121/1.419554.
[58] B. Masserey, P. Fromme, On the reflection of coupled Rayleigh-like waves at surface defects in plates, J. Acoust. Soc. Am. 123 (2008) 88–98, https://doi.org/10.1121/1.2805668.
[59] COMSOL Multiphysics Reference Manual 5, 2018 vol. 4, https://doc.comsol.com/5.4/doc/com.comsol.help.comsol/COMSOL_ReferenceManual.pdf.
[60] MATLAB, Curve fitting toolbox documentation. https://www.mathworks.com/help/curvefit/. (Accessed 17 January 2022) accessed.
[61] J.A. Parker, R.V. Kenyon, D.E. Troxel, Comparison of interpolating methods for image resampling, IEEE Trans. Med. Imag. 2 (1983) 31–39, https://doi.org/10.1109/TMI.1983.4307610.
[62] A. Rosenthal, D. Razansky, D. Soliman, G. Wissmeyer, H. Estrada, M. Seeger, R. Shnaiderman, V. Ntziachristos, Fiber interferometer for hybrid optical and optoacoustic intravital microscopy, Optica 4 (Issue 10) (2017) 1180–1187, https://doi.org/10.1364/OPTICA.4.001180, 1180–1187.
[63] T. Berer, I.A. Veres, H. Grün, J. Bauer-Marschallinger, K. Felbermayer, P. Burgholzer, Characterization of broadband fiber optic line detectors for photoacoustic tomography, J. Biophot. 5 (2012) 518–528, https://doi.org/10.1002/JBIO.201100110.
[64] G. Wild, S. Hinckley, Acousto-ultrasonic optical fiber sensors: overview and state-of-the-art, IEEE Sensor. J. 8 (2008) 1184–1193, https://doi.org/10.1109/JSEN.2008.926894.
[65] R.E. Silva, M.A. Franco, H. Bartelt, A.A.A.P. Pohl, Numerical characterization of an acousto-optic ring sensor for measuring D-Glucose concentrations, in: Work. Spec. Opt. Fibers Their Appl., OSA, Washington, D.C., 2013, https://doi.org/10.1364/WSOF.2013.F2.20. F2.20.

[66] A. Diez, G. Kakarantzas, T.A. Birks, P.S.J. Russell, Acoustic stop-bands in periodically microtapered optical fibers, Appl. Phys. Lett. 76 (2000) 3481, https://doi.org/10.1063/1.126684.
[67] D. Hu, H. Xuan, Z. Yu, D.Y. Wang, B. Liu, J. He, A. Wang, Acoustic fiber bragg grating and its application in high temperature sensing, IEEE Sensor. J. 18 (2018) 9576–9583, https://doi.org/10.1109/JSEN.2018.2867604.
[68] M. Delgado-Pinar, D. Zalvidea, A. Diez, P. Perez-Millan, M. Andres, Q-switching of an all-fiber laser by acousto-optic modulation of a fiber Bragg grating, Opt Express 14 (2006) 1106–1112, https://doi.org/10.1364/OE.14.001106.